Icarus 209 (2010) 230–238

Contents lists available at ScienceDirect

Icarus

journal homepage: www.elsevier.com/locate/icarus

The morphology of Mercury's Caloris basin as seen in MESSENGER stereo topographic models

Jürgen Oberst [a,*], Frank Preusker [a], Roger J. Phillips [b], Thomas R. Watters [c], James W. Head [d], Maria T. Zuber [e], Sean C. Solomon [f]

[a] German Aerospace Center, Institute of Planetary Research, D-12489 Berlin, Germany
[b] Planetary Science Directorate, Southwest Research Institute, Boulder, CO 80302, USA
[c] Center for Earth and Planetary Studies, National Air and Space Museum, Smithsonian Institution, Washington, DC 20560, USA
[d] Department of Geological Sciences, Brown University, Providence, RI 02912, USA
[e] Department of Earth, Atmospheric, and Planetary Sciences, Massachusetts Institute of Technology, Cambridge, MA 02139-4307, USA
[f] Department of Terrestrial Magnetism, Carnegie Institution of Washington, Washington, DC 20015, USA

ARTICLE INFO

Article history:
Received 30 October 2009
Revised 1 March 2010
Accepted 10 March 2010
Available online 16 March 2010

Keywords:
Mercury
Cratering
Geological processes

ABSTRACT

A digital terrain model (1000-m effective spatial resolution) of the Caloris basin, the largest well-characterized impact basin on Mercury, was produced from 208 stereo images obtained by the MESSENGER narrow-angle camera. The basin rim is far from uniform and is characterized by rugged terrain or knobby plains, often disrupted by craters and radial troughs. In some sectors, the rim is represented by a single marked elevation step, where height levels drop from the surroundings toward the basin interior by approximately 2 km. Two concentric rings, with radii of 690 km and 850 km, can be discerned in the topography. Several pre-Caloris basins and craters can be identified from the terrain model, suggesting that rugged pre-impact topography may have contributed to the varying characteristics of the Caloris rim. The basin interior is relatively smooth and shallow, comparable to typical lunar mascon mare basins, supporting the idea that Caloris was partially filled with lava after formation. The model displays long-wavelength undulations in topography across the basin interior, but these undulations cannot readily be related to pre-impact topography, volcanic construction, or post-volcanic uplift. Because errors in the long-wavelength topography of the model cannot be excluded, confirmation of these undulations must await data from MESSENGER's orbital mission phase.

1. Introduction

The Caloris basin (centered at 30°N, 165°E) was discovered in images obtained by Mariner 10 during its three flybys of Mercury in 1974–1975. Owing to the orbital resonance of Mercury and the spacecraft, the same hemisphere of the planet was imaged under similar illumination conditions during each flyby, and the Mariner 10 cameras were able to view only the eastern portion of Caloris. Images obtained during the first flyby of Mercury by the MErcury Surface, Space ENvironment, GEochemistry, and Ranging (MESSENGER) spacecraft (Solomon et al., 2008) show the basin at its full extent (Murchie et al., 2008; Fassett et al., 2009; Watters et al., 2009). Because of high Sun (low incidence) angles in the basin area, however, the images do not give much indication of the topographic relief and surface morphology. Moreover, craters with bright ejecta rays are abundant in the area and mask some of the details of the basin morphology. MESSENGER's onboard laser altimeter collected two elevation profiles, one during each of the first two Mercury flybys, but these were in near-equatorial areas (Zuber et al., 2008) and did not transect the Caloris basin area.

In this paper, we use stereo images obtained during the first MESSENGER flyby of Mercury to derive a topographic model of the Caloris basin, from which we examine the basin morphology in detail. At a basin ring diameter of 1550 km (Murchie et al., 2008; Fassett et al., 2009), Caloris is one of the largest impact basins known in the Solar System and among the youngest of the large impact basins on Mercury. Its structure is relevant to the processes of basin formation and subsequent modification. Additionally, the morphology of the basin reflects its volcanic and tectonic evolution and provides important constraints on the thermal state and mechanical properties of Mercury's crust and lithosphere over time.

2. Image data

2.1. Camera

The Mercury Dual Imaging System (MDIS) (Hawkins et al., 2007, 2009) consists of a pair of wide- and narrow-angle cameras,

* Corresponding author at: German Aerospace Center (DLR), Rutherfordstr. 2, D-12489 Berlin, Germany.
E-mail address: Juergen.Oberst@dlr.de (J. Oberst).

0019-1035/$ - see front matter © 2010 Elsevier Inc. All rights reserved.
doi:10.1016/j.icarus.2010.03.009

coaligned on a pivot platform. Both cameras are equipped with identical 1024 × 1024 format charge-coupled devices (CCDs) featuring 14-μm pixels and can deliver images with a pixel dynamic intensity range of 12 bits. Unlike the wide-angle camera (WAC), the narrow-angle camera (NAC) possesses a single filter only (700–800 nm). The NAC, featuring a compact off-axis optical system, suffers from geometrical distortions. Laboratory data from the ground as well as inflight stellar calibration data have been used to determine a geometric distortion map (F.S. Turner, personal communication, 2009), which has been utilized for this analysis. Indeed, once calibrated, CCD cameras are considered geometrically more stable than the Mariner 10 vidicon cameras and better suited for the photogrammetric measurement techniques central to this paper.

2.2. Images and mosaics

Image mosaics are obtained by scans of the pivot platform in combination with changes in the orientation of the spacecraft. This powerful capability was used to acquire several contiguous image mosaics during MESSENGER's first Mercury flyby (M1) on 14 January 2008 (Solomon et al., 2008). The digital terrain model (DTM) mosaic was produced from 208 NAC stereo images, which formed three sub-mosaics (H1, H2, and D1; Table 1).

The viewing geometry and the stereo conditions during the flybys were far from optimum, which aggravated DTM production. The basin was located near the planetary limb, and viewing (emission) angles near the northeastern margin of the basin were typically larger than 60°. Stereo angles were also small, differed substantially (8–14°) among respective image pairs, and were lowest (8°) for areas near the equator.

3. Stereo processing

The stereo processing follows algorithms and software realizations that have been used extensively on previous planetary image data sets (Albertz et al., 2005; Scholten et al., 2005; Heipke et al., 2007; Gwinner et al., 2009, 2010). However, adaptations of the software were required to account for MESSENGER camera parameters and image data formats. Also, software elements had to be combined in shell scripts. The processing had several stages, as described in the following.

3.1. Pointing data correction

The navigation data correction was carried out using bundle block adjustment techniques. This type of least-squares analysis produces solutions for spacecraft position and camera pointing for each image on the basis of large numbers of tie-point measurements. For the tie points, ground coordinates are computed in the process (Zhang et al., 1996). The a priori errors for angles were 450 μrad; errors in the spacecraft positions were assumed to be small (50 m).

Table 1
NAC sub-mosaics used to produce the DTM.

Mosaic	Time	No. of images	Resolution (m/pixel)
H1	E + 15 min	4 × 17	120–170
H2	E + 27 min	9 × 11	230–310
D1	E + 50 min	11 × 9	470–570

E (time of closest approach): 19:04 UTC, 14 January 2008. Time refers to first image taken.

First, the images were subjected to automatic image matching with a coarse matching grid to collect tie points. Only those tie points that were matched on at least three images were selected. In total, 21,975 line/sample coordinates were collected from the 208 images, representing 6475 ground points. Next, a starting model was derived. Three-dimensional Cartesian body-centered surface coordinates (x, y, z) of the tie points were computed from the nominal navigation data. While the horizontal coordinates were computed from classical ray intersections, the radius was kept fixed.

Next, full three-dimensional coordinates were derived by bundle block adjustment, beginning the iterations with the starting model. The inversion required solving the equations of observation for more than 24,500 unknowns (i.e., three spacecraft position components and three pointing angles for each image as well as three coordinates for each point). The adjustment converged after four iterations. Root mean square intersection errors were reduced from 10 km originally to 220 m. The intersection errors were visually inspected to verify that the model was free of stresses and topography bias. The high quality of the starting model prevented the iterations of the bundle block adjustment from converging erroneously on a local minimum of the residual field. Small errors in the starting model were found not to affect the outcome of the adjustment.

3.2. Image matching

Images were pre-rectified using the pointing data from the bundle block adjustment and subjected to automated image matching. A total of 241 individual matching runs were carried out on double- or triple-overlapping images. The pre-rectification step allowed searches for tie points to be limited to small areas. Hence, point misidentifications and gaps were reduced to a minimum.

3.3. Assembly of the DTM

Ray intersections of all matched points were computed to derive surface coordinates of object points. This process resulted in a total of 150 million object points. The object points were then interpolated to form a contiguous DTM grid at a size of 12.8 million pixels and a spatial resolution of 1000 m. While this spatial resolution is typically chosen to match the effective resolution of the model (a factor of three larger than the resolution of the images, according to a rule of thumb), a comparably small spatial resolution was chosen to avoid the loss of detail. No adjustments for absolute height or trend were applied. Though some erroneous height trend cannot be ruled out, gross errors in long-wavelength topography of the model are not likely, owing to the large number of concatenated images that are involved.

The DTM covers 12% of Mercury, or 8.8×10^6 km^2 (Fig. 1). Heights of the DTM are given with respect to a reference sphere of radius 2440 km. For further discussion, the portion of the object points that contained Caloris were extracted and projected separately onto a stereographic map (Fig. 2) centered on Caloris (30°N, 165°E). A variety of DTM representations were prepared, including the raw DTM (grey scale, Fig. 2), as well as shaded-relief maps color-coded by height (see Fig. 1 for an example). Selected height profiles were also computed for Caloris (Fig. 3) and areas of interest (Figs. 4–6).

The DTM has 8 km of total relief. The highest point within Caloris (2.5 km above the Mercury reference radius) is represented by an unnamed isolated peak (42.6°N, 149.9°E, Fig. 4). The lowest point within Caloris, and indeed of the DTM (5 km below the reference radius), is within the crater Atget in the southern basin floor (25.6°N, 166.4°E). At 100 km in diameter Atget is the largest crater within the Caloris basin (Fig. 5).

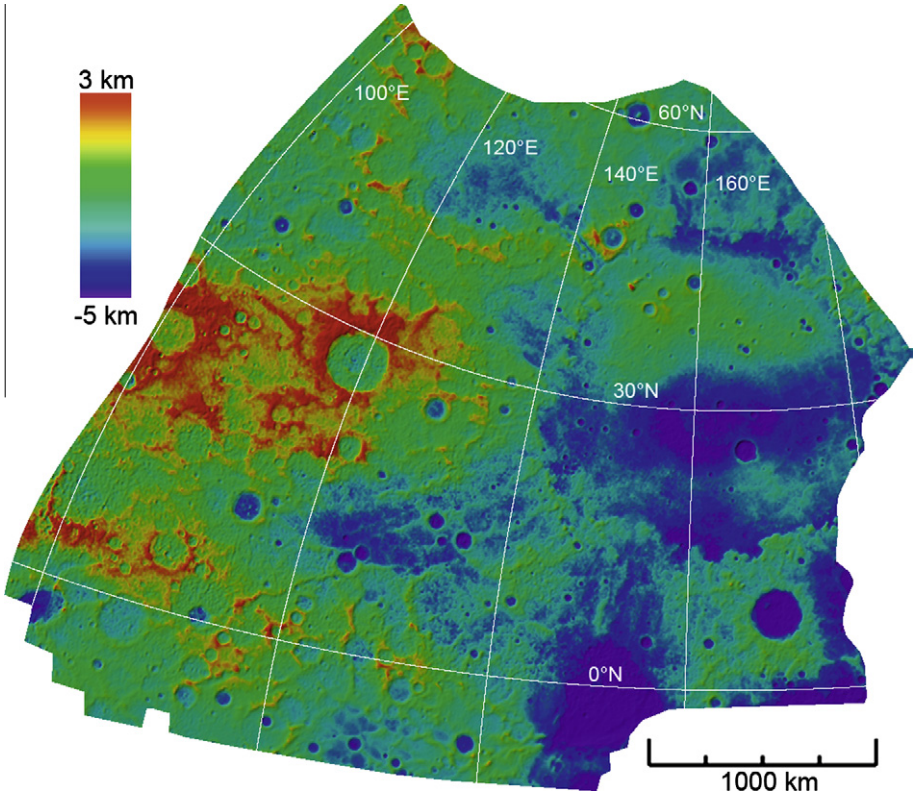

Fig. 1. Caloris area digital terrain model (DTM). The model has a grid size of 1000 m and covers an area of approximately 8.8×10^6 km^2. Heights are with respect to a sphere of radius 2440 km.

4. Basin morphology

The DTM is a rich source of information on diverse aspects of Caloris geology, in particular the Caloris basin rim, its ring structure, basin infilling, and possible pre-impact topography.

4.1. Basin rim-crest topography

The Caloris basin rim is well covered (except for parts of the southeastern sector, located beyond the planet limb) and can be clearly identified in the DTM. Along the northeastern margin, the rim is characterized by rugged massifs, which may represent what was identified as "Caloris Montes" in Mariner 10-based terrain classification schemes (Guest and Greeley, 1983; Spudis and Guest, 1988). These massifs have elevations above their surroundings of 1.5–3 km. Along the northwestern basin margin, the rim is represented by knobs within comparably smooth plains ("knobby plains"). Inspection of individual knobs indicates that these have typical horizontal scales of several kilometers and elevations of 1–2 km above their surroundings.

In other parts of the basin margin there is a lack of any obvious elevated ring structure at the resolution of the DTM. Rather, there appears to be a sudden drop from the surrounding elevation level toward the flat basin floor. This geometry is best seen along the meandering southern margin of the basin, where elevations fall from the surrounding terrain to the basin floor by 2–3 km over a linear distance of 20 km (Fig. 6). On the northern margin, the rim appears similar, but it is disrupted by craters and troughs.

Ridges and troughs oriented radially to the basin center disrupt the basin rim in several places. In the Mariner 10 classification schemes, these landforms have been grouped within the "Van Eyck Formation" (Guest and Greeley, 1983; Spudis and Guest, 1988; Fassett et al., 2009). The troughs represent a combination of secondary crater chains and graben that originated during basin formation. The most prominent of these features is located on the northwestern margin of Caloris [Fig. 4; see also Fig. 7a of Fassett et al. (2009)] and is characterized by two parallel troughs flanked by steep (5–6° slope) ridges on either side that extend for about 400 km and rise above the trough floors by approximately 2000 m (Fig. 4). Along the trough floor (Fig. 4, profile cc′), slopes cannot be distinguished from zero. The mean depth of the trough is 1.4 km below the reference datum.

4.2. Basin ring structure

Whereas the Mariner 10 images of the eastern margin suggested a diameter of the main Caloris basin ring of 1300 km (Guest and Greeley, 1983; Spudis and Guest, 1988), the MESSENGER images reveal a larger diameter of 1550 km (Murchie et al., 2008). Moreover, Fassett et al. (2009) argued for an elliptical shape for Caloris with long and short diameters of 1525 km and 1315 km, respectively.

Although the heavily eroded ring structure is difficult to identify in image data, owing to illumination conditions, the DTM gives us a fresh look at the basin structure. The DTM hints at residual ring structures in several areas (see arrows in Fig. 2 or rings in Fig. 7), but these features are not easily matched to other parts of a rim represented by a single circular or elliptical shape. An isolated chain of mountain peaks at the northwestern margin, the highest point within Caloris, is a prominent example (Fassett et al., 2009). We suggest that elevated topography of the basin rim region can be represented by two concentric circles, having diameters of 1380 km and 1700 km (Fig. 7). The mean of the two values (1540 km) agrees with the 1550-km diameter reported by

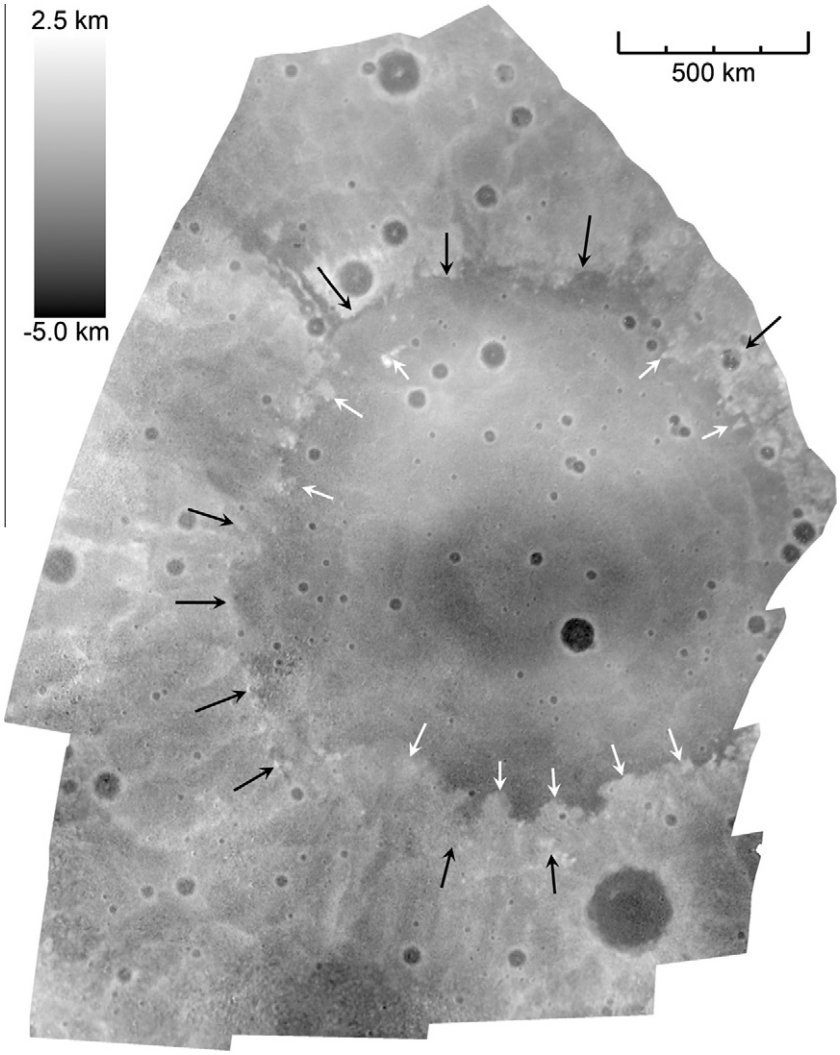

Fig. 2. Grey-scale representation of the Caloris basin DTM. Black and white arrows mark segments of the outer and inner rings, respectively, of the basin rim region.

Murchie et al. (2008). The two rings are centered at 31.7°N, 161.5°E.

There is further evidence for two or perhaps three circular concentric topographic highs within the basin (see Fig. 3, marked points A–C) at radii of approximately 315, 530, and 640 km, respectively. These highs represent modest variations in elevation with a horizontal scale of 50–100 km and with amplitudes of approximately 300 m. Although these highs can be difficult to identify in single profiles, the circular pattern becomes visible in the two-dimensional representation of the DTM. This pattern provides tentative confirmation of earlier suggestions of inner rings from Mariner 10 images (Spudis and Guest, 1988; Murchie et al., 2008). At the resolution and limited coverage of the DTM, we do not find clear evidence of rings outward of those identified here, as suggested by Spudis and Guest (1988) from Mariner 10 observations.

4.3. Pre-Caloris topography?

From inspection of the area around Caloris, it is difficult to determine a mean pre-impact elevation level, consistent with the possibility that the Caloris impactor hit rugged terrain with substantial topography in the form of pre-existing basins or large craters. We suggest that some of the Caloris basin-rim topography and its lack of continuity may be related to pre-Caloris topography. The rim structure shows significant asymmetry in level of preservation (see discussion above) as a function of radial range and sector, similar to what has been reported from studies of lunar impact basins, such as Imbrium (Head, 1982). From lunar studies it is known that where the pre-existing topography was large, the basin rim crest can be poorly developed. Some pre-Imbrium-basin lows are known to have influenced the subsequent Imbrium mare fill. We find traces of several pre-Caloris basins and smaller craters, tentatively marked in Fig. 7.

4.4. Caloris interior plains

The DTM provides critical data for assessing the nature of post-Caloris plains. It indicates that the interior topography of Caloris is smoother on average than its surroundings. Smooth areas follow the geologic boundaries of the basin rim. These characteristics support the idea that the interior of the basin was infilled by extensive volcanism (Murchie et al., 2008; Head et al., 2008).

It is instructive to compare the morphology of Caloris with those of lunar impact basins. Single profiles across prominent basins were selected from Clementine lunar topography (Smith

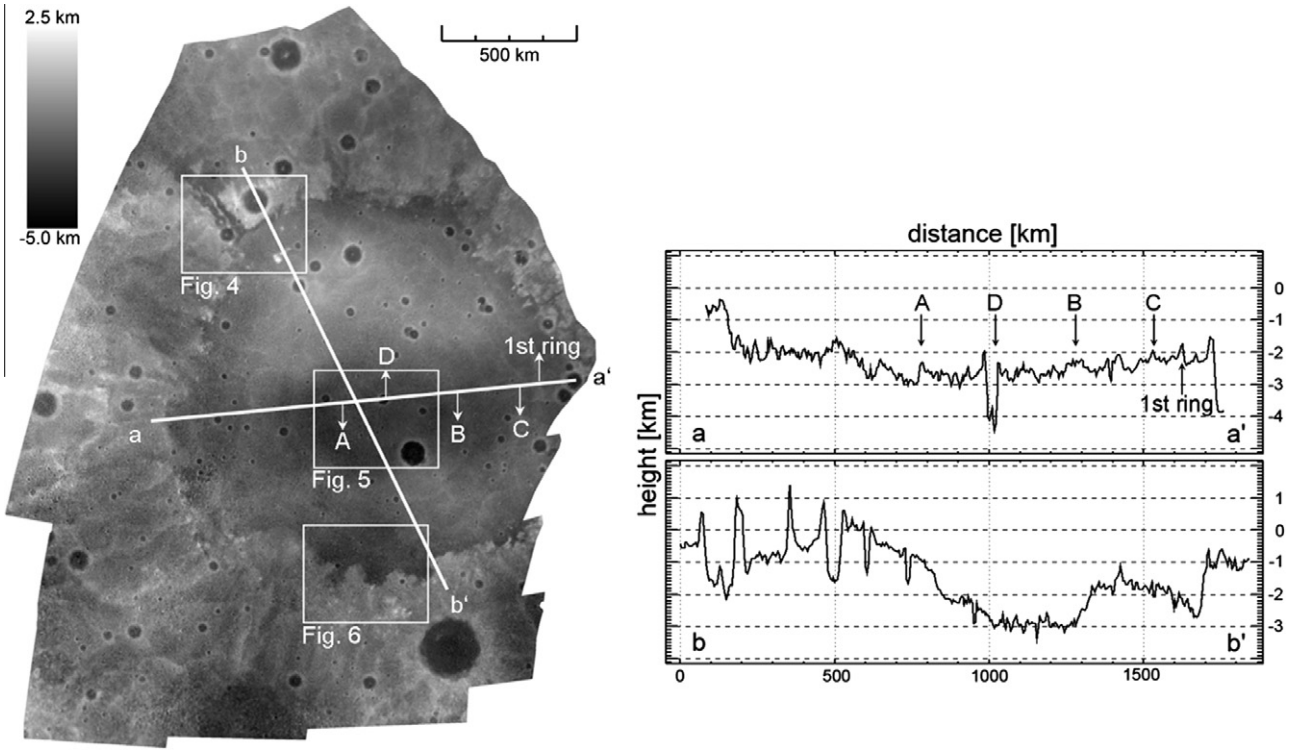

Fig. 3. Selected topographic profiles and locations of areas shown in greater detail in later figures (identified by figure number).

et al., 1997). Caloris is shallower than the lunar Orientale basin, which is similar in diameter but has a depth from rim crest to basin floor of 6 km (Fig. 8). The Caloris profile is more similar to those of Serenitatis and Imbrium, both of which are comparably shallow (approximately 1–2 km from rim crest to floor) and have flat basin floors (Fig. 8). Unlike Orientale, Serenitatis and Imbrium are filled with mare basalt to depths of several kilometers. The comparison suggests that Caloris was likewise infilled by large volumes of lava. While the resolution of Clementine data profiles are certainly limited, we suggest that further comparisons should be carried out using the vast volume of new altimeter data from lunar orbital missions now becoming available (Araki et al., 2009; Smith et al., 2010).

4.5. Long-wavelength topography

Within the Caloris basin interior, the DTM displays prominent long-wavelength variations in topographic height, particularly in the north–south direction (Fig. 3). A broad high dominates large parts of the northern basin floor and at its highest points exceeds

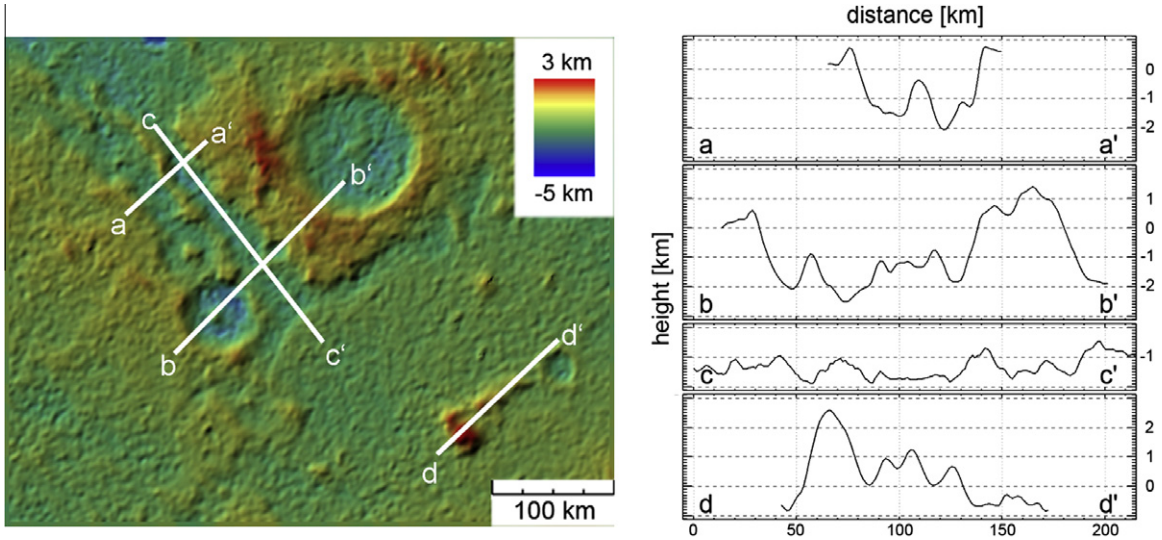

Fig. 4. Selected topographic profiles along and across a prominent trough located on the northwestern rim of, and radial to, the Caloris basin. The topographic high along profile dd′, interpreted as part of the inner Caloris basin ring, marks the highest point of the DTM.

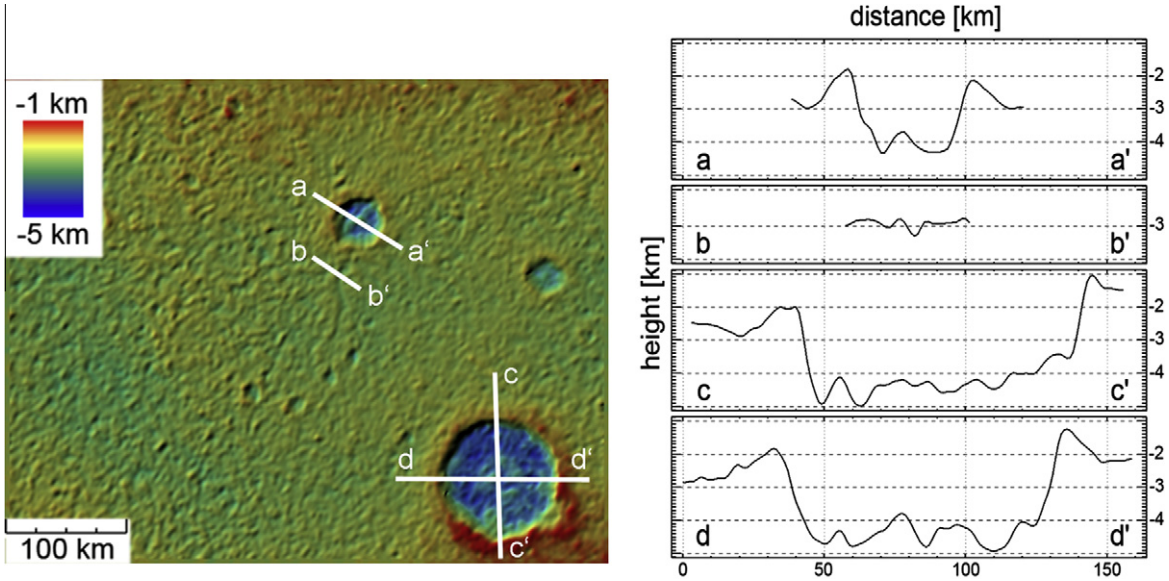

Fig. 5. Selected topographic profiles across Apollodorus (aa′) and Atget (cc′ and dd′) craters and a prominent trough (bb′) within the Pantheon Fossae graben complex. The interior of Atget marks the lowest point of the DTM.

the elevation of the basin rim by 1 km. A second, more modest high, seen in parts of the southern basin floor, is flanked by lows to the north and south (Fig. 3). The northern of those lows, which trends more or less east–west across the basin center, covers an area at least as large as the southern high. The magnitudes of these long-wavelength undulations in floor height reach 1–1.5 km (see profile bb′ in Fig. 3). It is possible that these topographic patterns are artifacts, as discussed below, but first we consider the basin floor topographic model at face value.

Physical mechanisms to account for the long-wavelength undulations in the Caloris basin floor displayed in the DTM are all problematic. One possibility is that the highs are relics of initially high topography in the pre-Caloris target area, perhaps smaller analogs of the extensive high region to the west of the basin (Fig. 1). The prominent Apennine–Archimedes area of the Imbrium basin provides an example of this scenario; the Archimedes plateau and the Apennine peaks remained high during later volcanic filling and constitute one of the least flooded areas of the Imbrium interior (Head, 1982). The Caloris interior is pervasively filled by plains material characterized by high reflectance and a steeper than average (or "redder") slope to the reflectance from visible to near-infrared wavelengths (Murchie et al., 2008; Robinson et al., 2008; Denevi et al., 2009). Sufficiently large younger craters in the basin floor have excavated low-reflectance material with shallower (or "bluer") spectral slope (Murchie et al., 2008; Denevi et al., 2009), indicating that such low-reflectance material underlies the high-reflectance plains at a depth of several kilometers (Ernst et al., 2010). There is no indication, however, that the thickness of high-reflectance plains is markedly less in areas of high floor topography on the DTM, as would be expected if such areas were also high prior to the time of volcanic infilling.

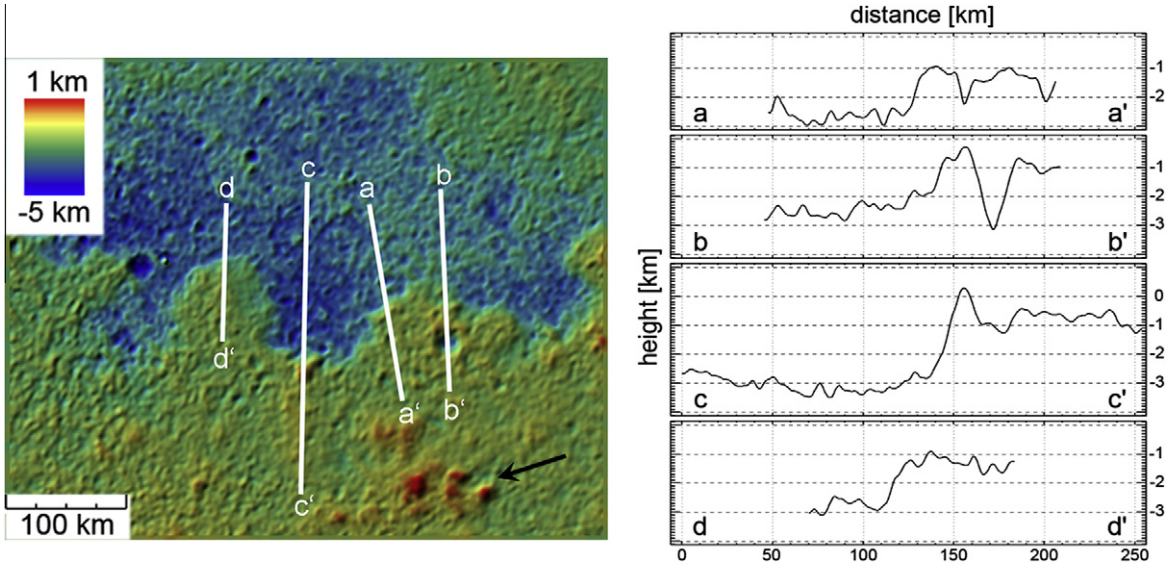

Fig. 6. Selected topographic profiles across the southern rim of the Caloris basin. Note the steep drop in elevation across the rim. The topographic feature marked by the black arrow is identified as part of the outer Caloris rim.

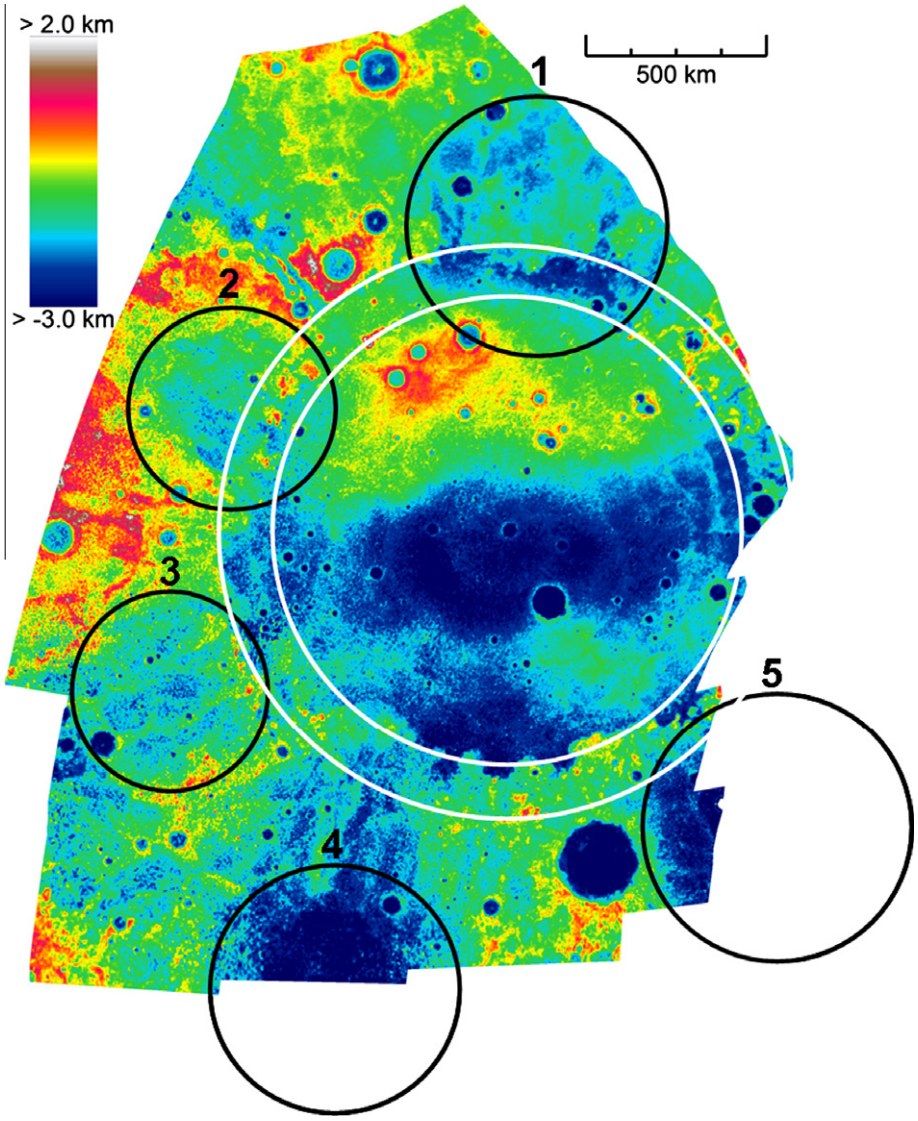

Fig. 7. Identification of Caloris basin rings (white) and tentative locations of large impact craters and basins (black) that predated the formation of Caloris, as inferred from the DTM. The two identified Caloris rings have radii of 690 and 850 km.

Two other possible mechanisms for the formation of highs within the Caloris basin floor are volcanic construction and uplift, but observations do not provide support for either. The high areas in the DTM lack evident volcanic source regions, and physical volcanological models for eruptions on Mercury favor high-effusion-rate eruptions that tend to produce broad plains rather than distinct edifices (Wilson and Head, 2008). Extensional fault structures, widespread within the interior of Caloris, provide ample evidence for floor uplift (Murchie et al., 2008; Watters et al., 2009), but the mapped distribution of extensional faults in the area does not show any correlation with the topographic highs in the DTM (Fig. 9). Notably, the large complex of radially oriented graben in the Pantheon Fossae area (see profile bb′ in Fig. 5 or marked point D in Fig. 3) are located within a central low in the DTM, opposite to the expectation if these structures formed in response to uplift by tectonic or magmatic processes (Murchie et al., 2008; Head et al., 2008; Watters et al., 2009).

5. Discussion

The DTM presented in this paper was determined solely on the basis of geometric (image disparity) effects and does not rely on assumptions regarding surface photometric properties. Owing to small stereo and oblique viewing angles for the available images, small errors in pointing angles and in the image matching will introduce comparatively large height errors, which we expect to correlate to some extent with the viewing geometry.

With some remaining errors in spacecraft navigation and camera calibration information, we cannot rule out offsets in absolute height and errors in long-wavelength trends in the model. It may be worthwhile to carry out a full study of the propagation of errors from navigation and camera parameters to the point accuracies for this particular imaging geometry with Monte Carlo techniques, but such an analysis is beyond the scope of this paper to perform. Owing to the large number of interlinked images, we nonetheless expect that the relative orientations of the images within the block are comparably stable. In addition, the analysis of residuals of control point coordinates does not show evidence of any "stresses" in the image block, i.e., displacements or vertical offsets of the individual DTM pieces. Consequently, any systematic errors within the model should be small.

It is important to assess whether the unusual long-wavelength topographic undulations within the floor of Caloris may be associated with errors in the long-wavelength stereo topography. To

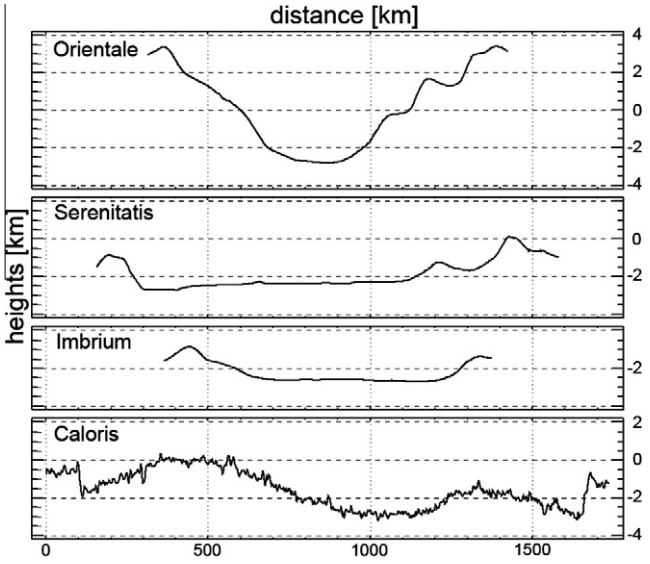

Fig. 8. Topographic profiles across selected lunar impact basins and Caloris. Lunar basin topography was taken from Clementine lidar data (Smith et al., 1997). Profiles pass through the basin centers and are in the north–south direction for the lunar basins; the profile for Caloris extends from northwest to southeast.

obtain an additional check, we investigated MESSENGER WAC images that were obtained during the same flyby. Though the wide-angle data are limited by low resolution, the data (with images taken through a different optical system and differently arranged footprints) hint at similar topographic patterns and trends. However, given the problems faced by physical mechanisms to account for the model's long-wavelength undulations across the Caloris basin floor, we suggest that this topic should await the acquisition of laser altimeter data from the Caloris area during MESSENGER's orbital mission phase.

The terrain model derived from MESSENGER stereo images gives us a fresh look at the morphology of Caloris and sets the stage for the observations of this largest impact basin on Mercury during MESSENGER's orbital mission phase. For the orbital phase of the mission, stereo sequences with global coverage from closer range and under appropriate lighting and viewing conditions are being planned. These observations will result in topographic models that improve the spatial resolution of the current Caloris model by a factor of two. With a more favorable viewing geometry, the noise in the terrain models will be substantially reduced and visibility into model details will be improved. Moreover, laser topographic profiles with their superior height precision will provide "ground truth" and calibration to reduce remaining ambiguities regarding absolute elevations and trends in long-wavelength topography.

Once data from the orbital mission phase are in hand, it will be worthwhile to study in detail the morphologies of other impact basins on Mercury to place Caloris into a global context. Comparisons of long-wavelength topography and gravitational anomaly observations obtained from MESSENGER radio tracking, together with high-resolution imaging and spectroscopy of geological units and tectonic features, will permit the large-scale structure and associated geological evolution of each of the larger basins to be discerned and compared.

Acknowledgments

We wish to thank two anonymous reviewers whose thoughtful comments improved this manuscript. The MESSENGER project is supported by the NASA Discovery Program under contracts NASW-00002 to the Carnegie Institution of Washington and NAS5-97271 to the Johns Hopkins University Applied Physics Laboratory.

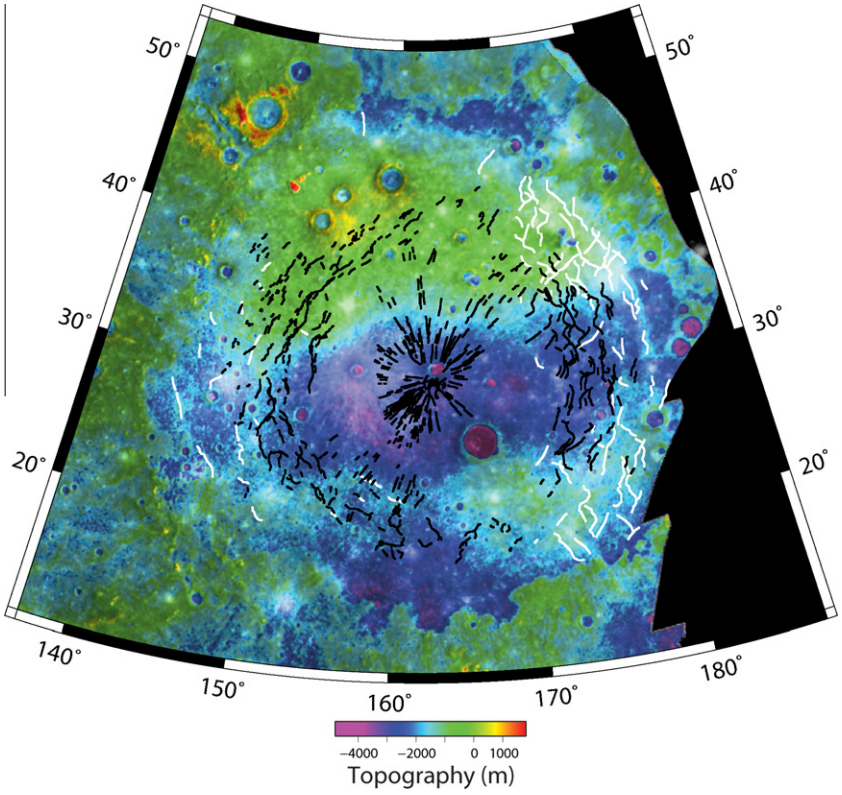

Fig. 9. Comparison of Caloris DTM with a map of prominent faults in the area, including graben (in black) and wrinkle ridges (in white) (Murchie et al., 2008; Watters et al., 2009).

References

Albertz, J., 24 colleagues, and the HRSC Co-Investigator Team, 2005. HRSC on Mars Express – Photogrammetric and cartographic research. Photogramm. Eng. Remote Sens. 71, 1153–1166.

Araki, H., and 10 colleagues, 2009. Lunar global shape and polar topography derived from Kaguya-LALT laser altimetry. Science 323, 897–900.

Denevi, B.W., and 10 colleagues, 2009. The evolution of Mercury's crust: A global perspective from MESSENGER. Science 324, 613–618.

Ernst, C.M., Murchie, S.L., Barnouin-Jha, O.S., Robinson, M.S., Denevi, B.W., Blewett, D.T., Head, J.W., Izenberg, N.R., Solomon, S.C., 2010. Exposure of spectrally distinct material by impact craters on Mercury: Implications for global stratigraphy. Icarus, in this issue.

Fassett, C.I., Head, J.W., Blewett, D.T., Chapman, C.R., Dickson, J.L., Murchie, S.L., Solomon, S.C., Watters, T.R., 2009. Caloris impact basin: Exterior geomorphology, stratigraphy, morphometry, radial sculpture, and smooth plains deposits. Earth Planet. Sci. Lett. 285, 297–308.

Guest, J.E., Greeley, R., 1983. Geologic map of the Shakespeare quadrangle of Mercury. Map I-1408, Misc. Investigations Ser., US Geological Survey, Denver, Colo.

Gwinner, K., Scholten, F., Spiegel, M., Schmidt, R., Giese, B., Oberst, J., Jaumann, R., Heipke, C., Neukum, G., 2009. Derivation and validation of high-resolution digital terrain models from Mars Express HRSC-data. Photogramm. Eng. Remote Sens. 75, 1127–1142.

Gwinner, K., Scholten, F., Preusker, F., Elgner, S., Roatsch, T., Spiegel, M., Schmidt, R., Oberst, J., Jaumann, R., Heipke, C., 2010. Topography of Mars from global mapping by HRSC high-resolution digital terrain models and orthoimages: Characteristics and performance. Earth Planet. Sci. Lett. 294, 506–519.

Hawkins III, S.E., and 24 colleagues, 2007. The Mercury Dual Imaging System on the MESSENGER spacecraft. Space Sci. Rev. 131, 247–338.

Hawkins III, S.E., and 18 colleagues, 2009. In-flight performance of MESSENGER's Mercury Dual Imaging System. In: X-ray, UV, Visible, and IR Instrumentation for Planetary Missions, SPIE International Symposium on Optical Engineering and Applications, Paper 7441A-3, 12pp. San Diego, CA, August 2–6, 2009.

Head, J.W., 1982. Lava flooding of ancient planetary crusts – Geometry, thickness, and volumes of flooded lunar impact basins. Moon Planets 26, 61–88.

Head, J.W., and 10 colleagues, 2008. Volcanism on Mercury: Evidence from the first MESSENGER flyby. Science 321, 69–72.

Heipke, C., 21 colleagues, and the HRSC Co-Investigator Team, 2007. Evaluating planetary digital terrain models – The HRSC DTM test. Planet. Space Sci. 55, 2173–2191.

Murchie, S.L., Watters, T.R., Robinson, M.S., Head, J.W., Chapman, C.R., Solomon, S.C., McClintock, W.E., Prockter, L.M., Domingue, D.L., Blewett, D.T., 2008. Geology of the Caloris basin, Mercury: A view from MESSENGER. Science 321, 73–76.

Robinson, M.S., and 12 colleagues, 2008. Reflectance and color variations on Mercury: Regolith processes and compositional heterogeneity. Science 321, 66–69.

Scholten, F., Gwinner, K., Roatsch, T., Matz, K.-D., Wählisch, M., Giese, B., Oberst, J., Jaumann, R., Neukum, G., and the HRSC Co-Investigator Team, 2005. Mars Express HRSC data processing – Methods and operational aspects. Photogramm. Eng. Remote Sens. 71, 1143–1152.

Smith, D.E., Zuber, M.T., Neumann, G.A., Lemoine, F.G., 1997. The global topography of the Moon from the Clementine lidar. 1997. J. Geophys. Res. 102, 1591–1611.

Smith, D.E., Zuber, M.T., Neumann, G.A., Lemoine, F.G., Mazarico, E., Torrence, M.H., Duxbury, T.H., Head III, J., and the LOLA Science and Instrument Team, 2010. LOLA observations of the Moon. Lunar Planet. Sci. 41. Abstract 1993.

Solomon, S.C., and 10 colleagues, 2008. Return to Mercury: A global perspective on MESSENGER's first Mercury flyby. Science 321, 59–62.

Spudis, P.D., Guest, J.E., 1988. Stratigraphy and geologic history of Mercury. In: Vilas, F., Chapman, C.R., Matthews, M.S. (Eds.), Mercury. University of Arizona Press, Tucson, pp. 118–164.

Watters, T.R., Murchie, S.L., Robinson, M.S., Solomon, S.C., Denevi, B.W., André, S.L., Head, J.W., 2009. Emplacement and tectonic deformation of smooth plains in the Caloris basin, Mercury. Earth Planet. Sci. Lett. 285, 309–319.

Wilson, L., Head, J.W., 2008. Volcanism on Mercury: A new model for the history of magma ascent and eruption. Geophys. Res. Lett. 35. L23205. doi:10.1029/2008GL035860.

Zhang, W., Giese, B., Oberst, J., Jaumann, R., 1996. Methods of the bundle block adjustment of planetary image data. Int. Arch. Photogramm. Remote Sens. 31, 1004–1009.

Zuber, M.T., and 13 colleagues, 2008. Laser altimeter observations from MESSENGER's first Mercury flyby. Science 321, 77–79.